

1,2-diol dehydration by the radical SAM enzyme AprD4 – a matter of proton circulation and substrate flexibility

Wan-Qiu Liu,^{†,§} Patricia Amara,^{‡,§} Jean-Marie Mouesca,[‡] Xinjian Ji,[†] Oriane Renoux,[‡]
Lydie Martin,[‡] Chen Zhang,[†] Qi Zhang^{†*} and Yvain Nicolet^{‡*}

[†] Department of Chemistry, Fudan University, Shanghai, China

[‡] Univ. Grenoble Alpes, CEA, CNRS, IBS, Metalloproteins, F-38000 Grenoble, France

[‡] Univ. Grenoble Alpes, CEA, CNRS, INAC, SyMMES, F-38000 Grenoble, France

[§] These authors contributed equally to this work

* qizhang@sioc.ac.cn and yvain.nicolet@ibs.fr

Table of contents

Figure S1.....	S2
Figure S2.....	S3
Figure S3.....	S4
Figure S4.....	S4
Figure S5.....	S5
Figure S6.....	S5
Figure S7.....	S6
Figure S8.....	S6
Figure S9.....	S7
Figure S10.....	S8
Figure S11.....	S8
Figure S12.....	S9
Table S1.....	S10
Material and Methods.....	S11
Biochemical analysis.....	S11
Crystallization and X-ray data collection.....	S11
X-ray structure determination.....	S12
Site-directed mutagenesis.....	S13
Computational studies (methods and results).....	S14
References.....	S20

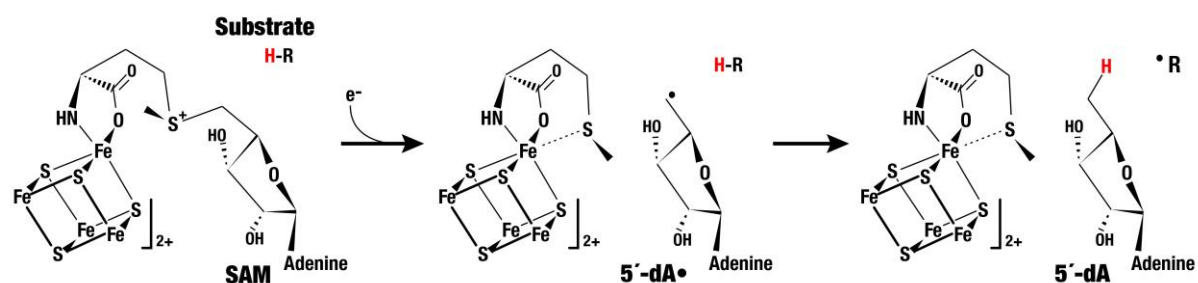


Figure S1. General mechanism of the radical SAM enzymes involving SAM cleavage to produce a 5'-dA• radical. The latter will subsequently activate the substrate of the enzyme.

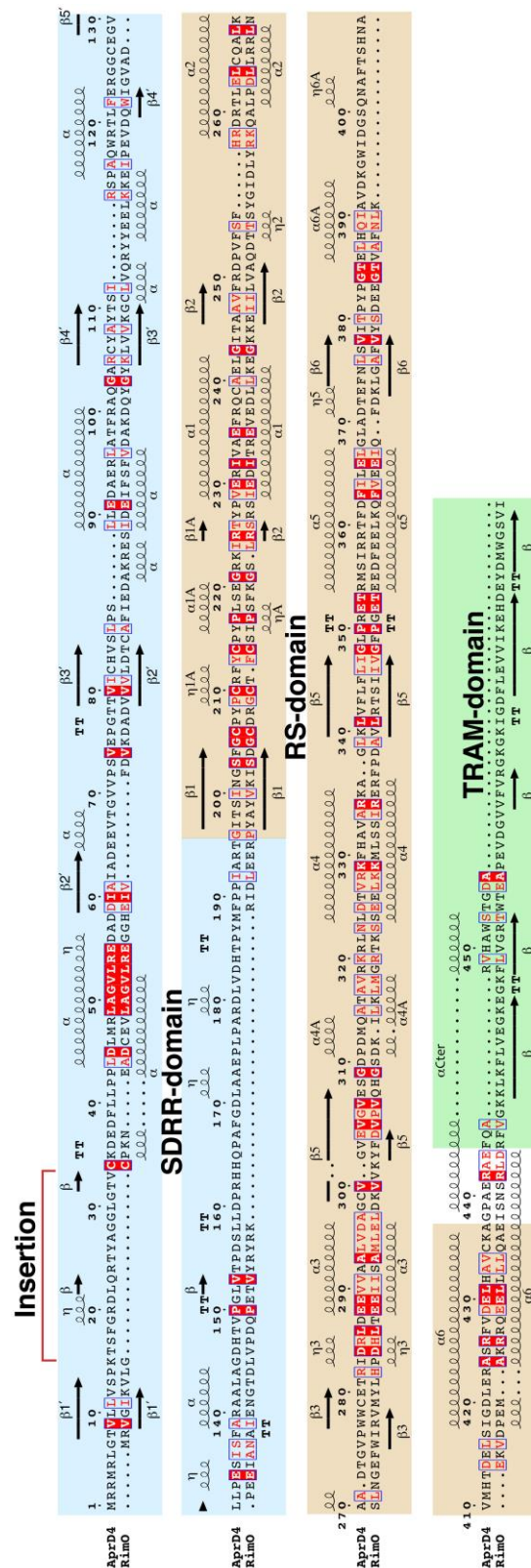


Figure S2. Comparison between AprD4 and RimO and the Single Domain Response Regulator. Structure-based amino-acid sequence alignment of AprD4 from *S. tenebrarius* and RimO from *T. maritima*.¹ The sequences corresponding to the SDRR domains are highlighted in blue. The ones corresponding to the radical SAM domain are highlighted in light brown and the TRAM domain specific to RimO in green.

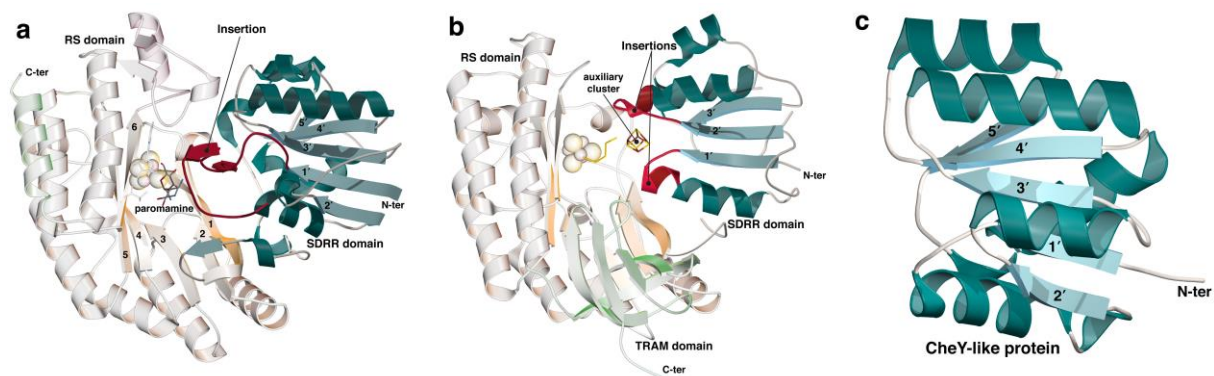


Figure S3. **a**, X-ray structure of AprD4. The SDRR domain is shown in blue while the rest of the structure is depicted in faded colors. β -strands are numbered according to their order in the amino acid sequence (primes are used for those of the SDRR domain). The SDRR insertion, which surrounds paromamine is depicted in red. **b**, RimO structure¹ (PDB code: 4JC0) same color code as in Figure S2. The two insertions responsible for the binding of the auxiliary cluster are depicted in red. **c**, X-ray structure of a CheY-like protein from *Thermotoga maritima* (PDB code: 2QXY).

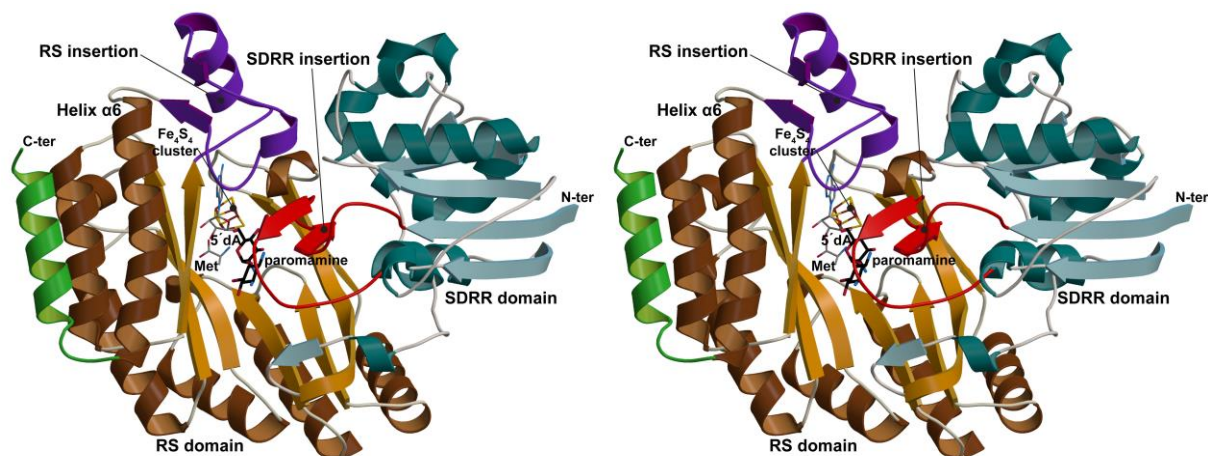


Figure S4. Stereo view of Figure 2a.

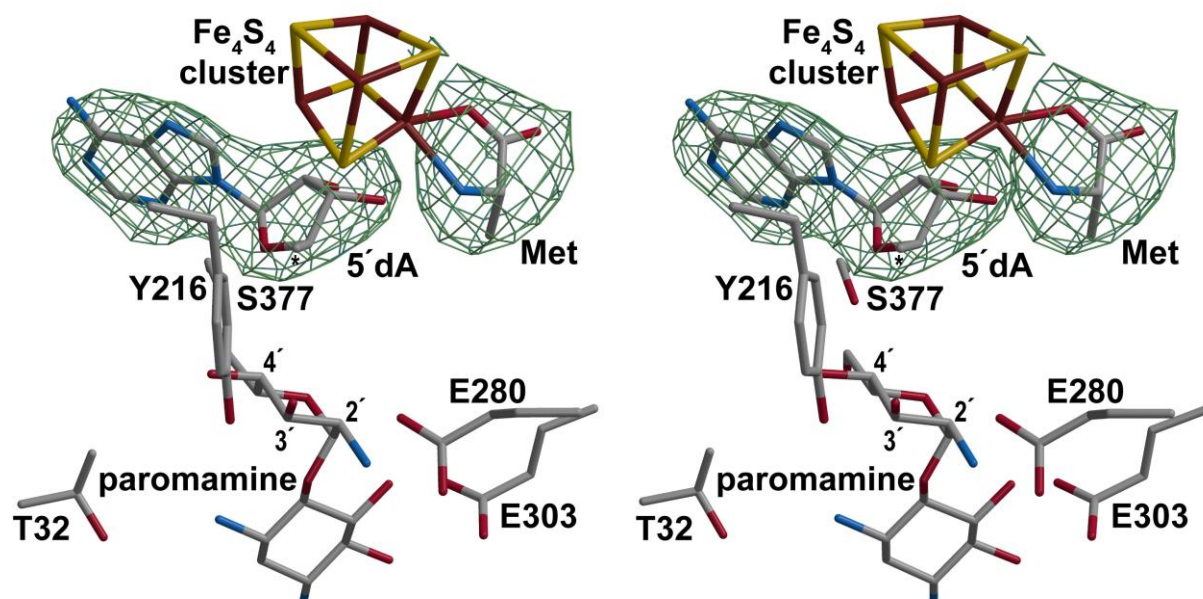


Figure S7. Stereo view of the difference Fourier electron density map around 5'dA and the Met fragment. The *F_o-F_c* electron density (omit map) is shown as a green mesh (contour 3 σ , cover radius 2.0 Å).

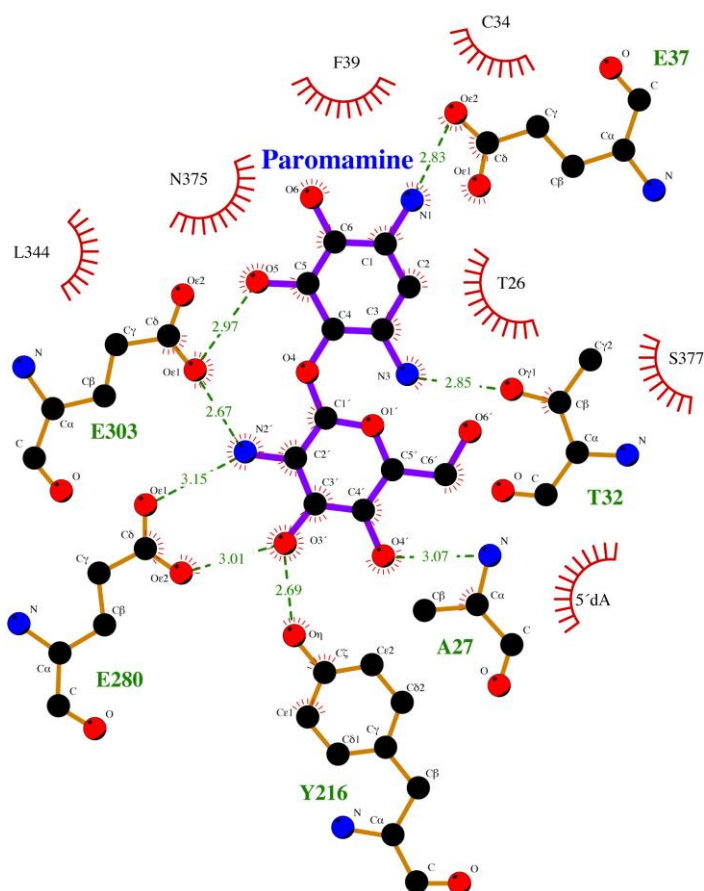


Figure S8. Ligplot of paromamine bound to the AprD4 active site (see Figure 2d).

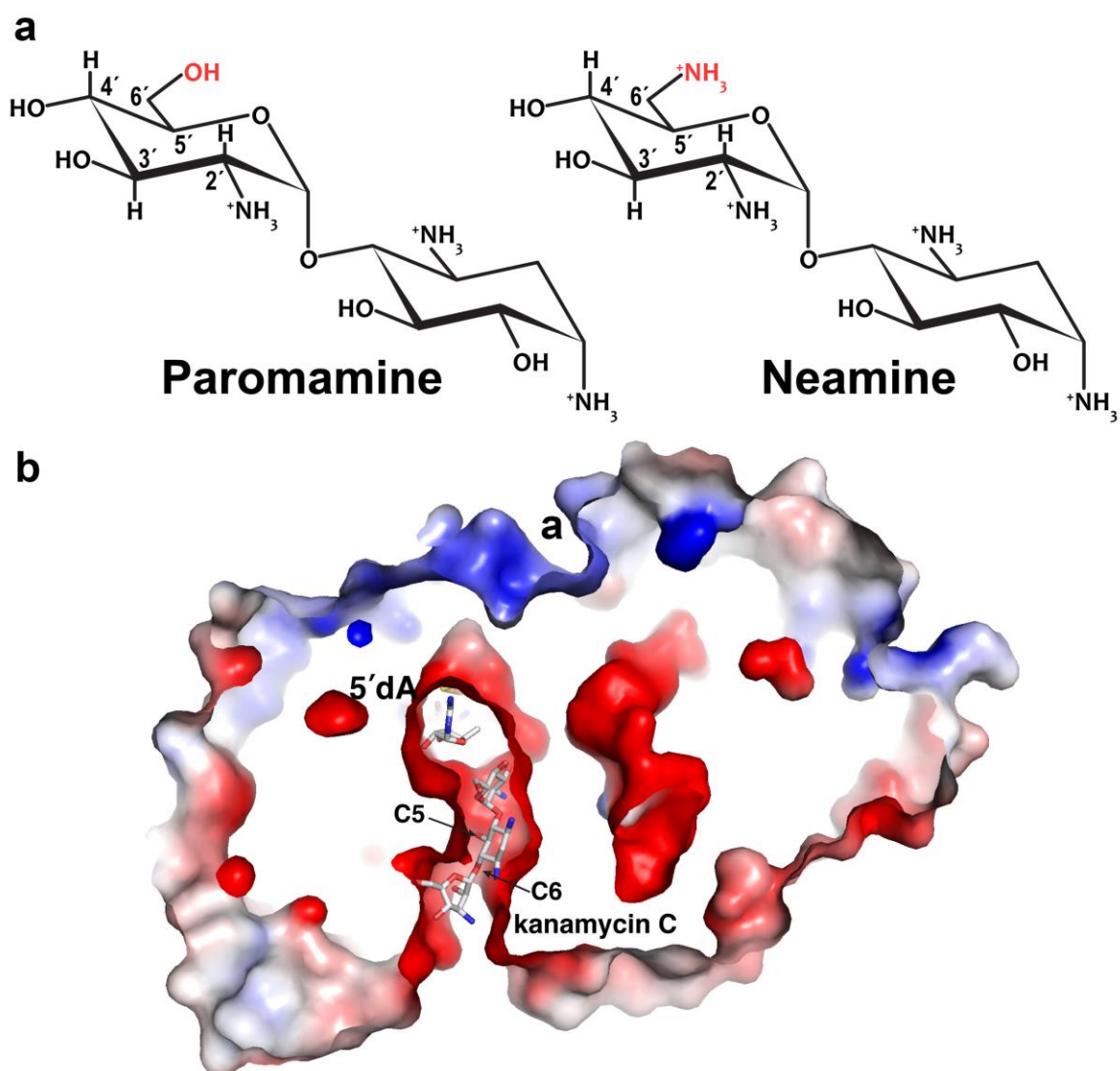


Figure S9. **a**, Chemical representation of paromamine and neamine. **b**, Cross-section of the electrostatic potential surface (red: negative; blue: positive) surrounding the active site cavity. A manually-docked model of kanamycin C, based on the structure of the bound paromamine, illustrates the capability of AprD4 to accommodate various substrates substituted at the C6 atom of the 2-DOS. Conversely, the C5 atom points toward a crowded region explaining why the protein cannot accommodate C5-substituted 2-DOS analogs.

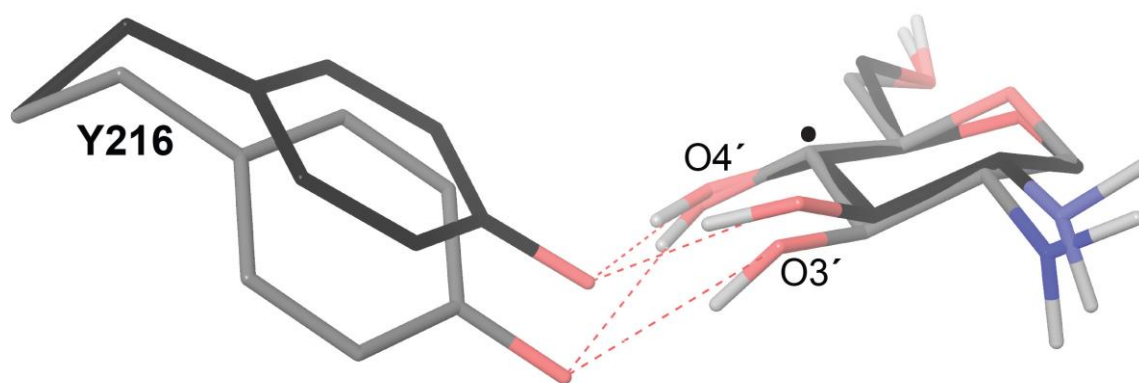


Figure S10. Close-up of the Y216 movement and its abstraction of a proton at O4'. Only the D-glucosamine part of the substrate is represented for clarity (see main text and Figure 3).

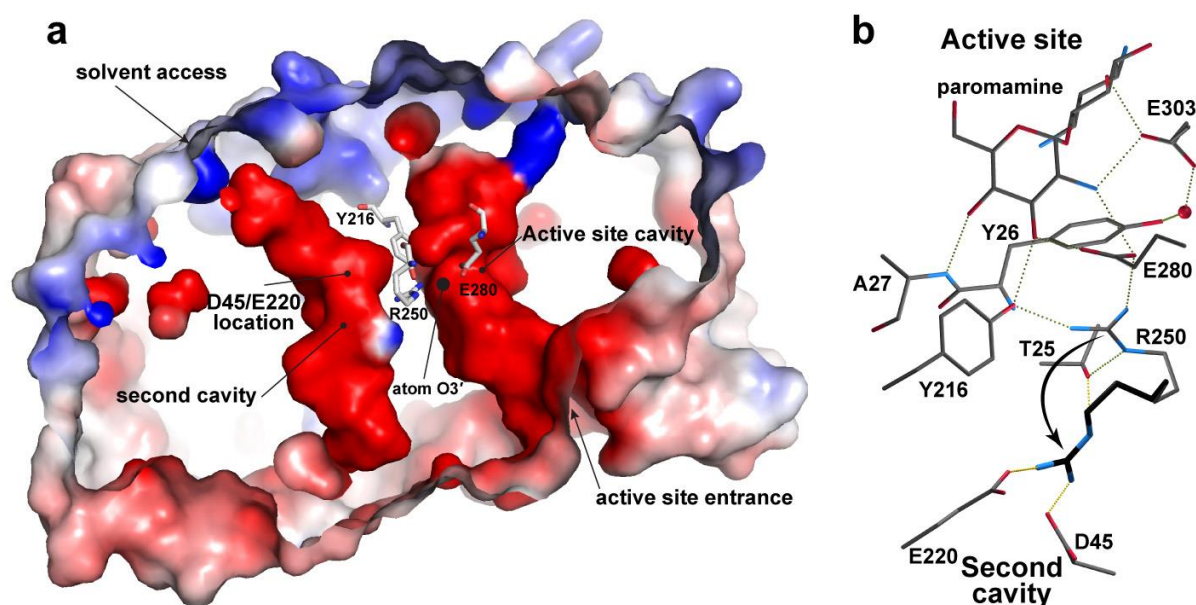


Figure S11. Second cavity and water release. **a**, Cross-section of the electrostatic potential surface with the two cavities depicted. **b**, Putative movement of the R250 residue from the active site to the E220/D45 gripper in the second cavity. Such movement connects the two cavities and may serve as a pathway for the egress of the water molecule released during the reaction.

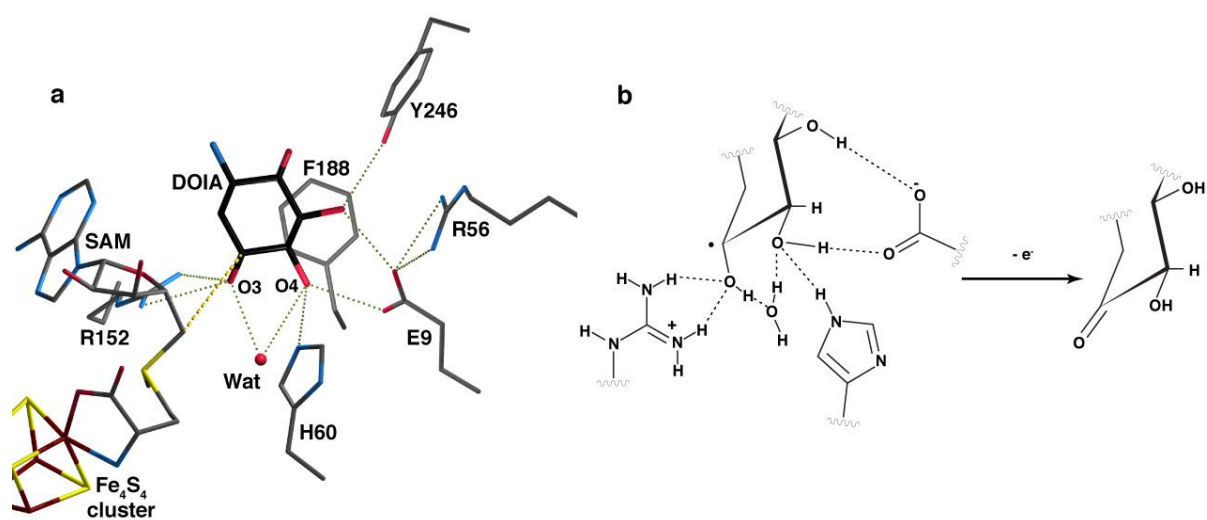


Figure S12. Active site of the radical SAM enzyme BtrN. **a**, The environment of the substrate 2-deoxy-scylo-inosamine (DOIA).² **b**, reaction catalyzed by BtrN starting from the substrate radical intermediate.

Table S1. Data collection, phasing and refinement statistics

	Crystal 1			Crystal 2			5'dA + Methionine + Paromamine complex structure		
Data collection	<i>P</i> 3 ₁ 21			<i>P</i> 3 ₁ 21			<i>P</i> 3 ₁ 21		
Space group	<i>P</i> 3 ₁ 21			<i>P</i> 3 ₁ 21			<i>P</i> 3 ₁ 21		
Cell dimensions									
<i>a b c</i> (Å)	121.6	121.6	234.9	123.4	123.4	233.7	121.8	121.8	233.8
$\alpha \beta \gamma$ (°)	90	90	120	90	90	120	90	90	120
Wavelength (Å)	1.7304 (Peak)	1.7439 (Inflection)	0.8729 (Remote)	1.0723			0.9724		
Resolution (Å) ^a	3.5 (3.59-3.5)	3.5 (3.59-3.5)	3.2 (3.28-3.2)	2.8 (2.87-2.8)			2.55 (2.62-2.55)		
<i>R</i> _{sym} (%)	15.7 (140)	17.6 (192)	11.9 (145)	5.9 (186)			7.8 (71)		
<i>I</i> / σ (<i>I</i>)	11.98 (1.2)	11.06 (0.86)	9.98 (0.83)	14.31 (0.65)			9.77 (1.45)		
<i>CC</i> _{1/2} (%)	99.6 (73.7)	99.6 (62.1)	99.7 (50.2)	99.9 (19.4)			99.9 (24.4)		
Completeness (%)	99.8 (97.8)	99.9 (99.2)	95.5 (96.7)	99.1 (99.1)			98.4 (87.0)		
Redundancy	5.73 (5.6)	5.72 (5.3)	3.86 (3.9)	3.38 (3.4)			3.39 (2.6)		
Refinement									
Resolution (Å)							2.55		
No. reflections							65660		
<i>R</i> _{work} / <i>R</i> _{free}							0.227 (0.262)		
No. atoms							7161		
Protein							7010		
Fe ₄ S ₄ clusters							16		
Paromamine							44		
5'dA							36		
Methionine							12		
Water							43		
<i>B</i> factors (Å ²)									
Protein							95.23		
Fe ₄ S ₄ clusters							71.84		
Paromamine							78.42		
5'dA							85.37		
Methionine							68.05		
Water							73.84		
r.m.s deviations									
Bond lengths (Å)							0.006		
Bond angles (°)							0.982		

^a Values in parentheses are for the highest-resolution shell.

Biochemical analysis

Protein overexpression and purification, and chemical reconstitution of the FeS cluster of AprD4 and its mutants were performed as previously described.³ A typical AprD4 reaction was performed by incubating 200 μ M paromamine with ca. 50 μ M reconstituted AprD4 and 4 mM sodium dithionite in 50 mM MOPS buffer (pH 8.0) at room temperature for 10 min, and the reaction was initiated by the addition of SAM to a final concentration of 1 mM. The reaction mixtures were incubated at room temperature for 4-5 h, and the reactions were terminated by addition of trichloroacetic acid (TCA) to a final concentration of 10% (v/v). After removal of the protein precipitates by centrifugation, the supernatant was subjected to LC-MS analysis.

To quantify the dehydratase activity of AprD4 and its mutants, we performed the AprD4/AprD3 coupled reaction by incubating 500 μ M paromamine with ca. 50 μ M reconstituted AprD4, ca. 50 μ M AprD3, 1 mM SAM, 1 mM NADPH, and 4 mM sodium dithionite in 50 mM MOPS buffer (pH 8.0). The reaction mixtures were incubated at room temperature for 2 h and were terminated by TCA addition. Enzyme activities were quantified by selectively monitoring the intensity of the MS/MS fragmentation ion $m/z = 163.1$ of lividamine **3** produced in the reaction, with the remaining paromamine as the internal standard.

Crystallization and X-ray data collection

The protein (10 mg/mL in 50 mM MOPS, 25 mM NaCl, 10 mM DTT and 10% (v/v) glycerol, pH 8.0) was first incubated with 6-fold excess 5'-deoxyadenosine and methionine and 3-fold excess paromamine for 30 minutes prior to setting up the crystallization trials. Initial crystallization conditions (20% polyethylene glycol (PEG) 6000; 0.1 M MES buffer pH 6) were obtained using commercial sparse matrix screens and our automated crystallization robot (Gryphon – Art-Robbin Inst.) under anaerobic conditions. They were subsequently manually optimized to 20% PEG 6000; 0.1 M MES pH 6; 5% PEG 400). Brown crystals that appeared within three weeks, were mounted in a cryo-loop after a quick soak in a solution containing 25% PEG 6000; 0.1 M MES pH 6; 5% PEG 400; 20% glycerol and were frozen directly in the glove box using liquid propane.⁴ All the X-ray data collections were collected on beamlines at the European Synchrotron Radiation Facility (ESRF). Crystal 1 was used to collect a multiwavelength anomalous dispersion (MAD) dataset at three wavelengths (Table S1). The remote wavelength was collected on beamline ID23-eh2, whereas the inflection and peak datasets were collected on beamline BM30a. Datasets for crystal 2 and AprD4-5'dA-methionine complex were collected on beamlines ID29 and ID23-eh1, respectively. X-ray data were processed using XDS⁵ and further scaled using XSCALE. We paid a special attention to use the same set of reflections as an R_{free} test set between the different datasets.⁶ Statistics for data processing are presented in Table S1.

X-ray structure determination

The AprD4 X-ray structure was determined by a combination of the multi-wavelength anomalous dispersion (MAD) and molecular replacement methods completed with extensive density modification procedures. This led an X-ray structure corresponding to the 5'dA + methionine complex with paromamine bound, at 2.55 Å resolution, respectively. The model corresponds to two molecules per asymmetric unit with molecule A including residues 4 to 457 and molecule B, residues 5 to 457. Both molecules contain one Fe₄S₄ cluster, one molecule of paromamine and one molecule of 5'dA + methionine, with $R_{\text{free}} = 0.262$ (Table S1). Surfaces and Assemblies (PISA) server⁷ indicates that physiologically, AprD4 is monomeric.

Due to the low resolution and the relatively poor anomalous signal extracted from the peak and inflection datasets, we first searched the iron atoms considering the whole Fe₄S₄ cluster as a super-atom that was best modelled as plutonium. Anomalous peak search and initial density modification were carried out using SHELXCDE⁸ implemented in HKL2MAP.⁹ Only two sites were identified, suggesting only two AprD4 molecules per asymmetric unit (one Fe₄S₄ cluster/protein) with a solvent content of over 70% with a $V_m = 6.14$.¹⁰ While still poor, the resulting electron density map exhibited features that were best identified as α -helices and the largest peak corresponding to the Fe₄S₄ cluster surrounded by cysteine residues. We subsequently superimposed all the radical SAM enzymes structures available in the Protein Data Bank and selected only their radical SAM domain. Each of them was manually placed in the electron density map, with the Fe₄S₄ cluster located into the highest peak and was subsequently manually rotated in order to fit the α -helices into the remaining electron density. Of all the models tested, only one, the radical SAM domain from RimO (PDB code 4JC0)¹ gave a fit for most of its α -helices and β -strands. After placing the two RimO fragments (converted into poly Ala chains) in the electron density we manually corrected the orientation of the α -helices, leading to a starting model. Subsequently, combining this model and the experimental electron density map (see above) we performed a cycle of automated building and density modification, including solvent flattening and 2-fold non-crystallographic symmetry averaging using AUTOBUILD from PHENIX.¹¹ The resulting electron density map was used to further correct manually the model and to progressively build the missing parts. After several cycles of this protocol, a nearly complete model with $R_{\text{free}} = 0.305$ (3.2 Å resolution) was obtained.

At this stage, using dataset from crystal 2, classical refinement (PHENIX REFINE) and manual building cycles were carried out leading to a final model corresponding to residues 4 to 457 for molecule A and 5 to 457 for molecule B, with $R_{\text{free}} = 0.254$. Subsequently, a higher resolution dataset (5'dA + Met + paromamine complex) was obtained and used, leading to the final structure presented here (Table S1). Residual electron density observed in the active site around the FeS cluster in

both molecules A and B was best modelled by paromamine (Figure 2b) and 5'dA + Met molecules. Only the alanyl part of methionine could be clearly modelled, suggesting that the side chain is disordered and does not bind as tightly as previously observed in other radical SAM enzymes.^{12,13} The structure exhibits more than 93% of the residues in the most favored regions of the Ramachandran plot¹⁴ and less than 0.5% in the unfavorable ones. Its overall Molprobity scores is 2.92.¹⁵

Using the Feature-Enhanced Map calculation,¹⁶ additional electron density corresponding to a third AprD4 molecule partially disordered was observed in all datasets. Such extra electron density was not present in the difference Fourier maps with the only exception of the region around the Fe₄S₄ cluster. However, no peak was observed in this region in the anomalous difference maps, supporting a very weak contribution of this molecule to the structure factors due to the high disorder. Furthermore, despite many attempts to model parts of this supplementary molecule, no improvement of the statistics was observed. As it only poorly contributes to diffraction and that maintaining a correct geometry for this third molecule was extremely difficult without degrading the other two, which are better defined, it has been decided to remove it from final models. Molecular assembly analysis using the Proteins, Interfaces, Surfaces and Assemblies (PISA) server⁷ indicates that despite the 3 molecules per asymmetric unit content, AprD4 is a monomer.

Site-directed mutagenesis

Constructs for overexpression of AprD4 mutants were made by using the one-step site-directed mutagenesis method. Briefly, two fragments were amplified from the plasmid AprD4-pET28a³ by using a primer pair *AprD4-F1* and *AprD4-mutant-R* (e.g. AprD4-E280Q-R for making the E280Q mutant), and a second primer pair *AprD4-mutant-F* and *AprD4-R* (See table below). The resulting two PCR products were cloned into pET28a by homologous recombination using ClonExpress MultiS One Step Cloning Kit (Vazyme Biotech Co., Ltd) by following the manufacturer's instructions. Typically, 20 µL reaction mixture containing 4 µL 5×CE MultiS Buffer, 2 µL Exnase MultiS, ~50 ng linear pET28a plasmid (pre-digested with NdeI/XhoI), ~20 ng fragment 1, ~20 ng fragment 2 and ddH₂O, was incubated at 37°C for 30 min. Chemically competent *E. coli* DH5α cells were transformed with the ligation mixture and plated on LB-agar containing kanamycin (50 µg/mL) to screen for positive clones, which were confirmed by DNA sequencing. To make the D45N/E220Q double mutant, we first constructed the E220Q mutant and then made the double mutant from E220Q.

Primers for AprD4 site-directed mutagenesis.

Primer	Sequence (5'-3')
<i>AprD4-F</i>	ccgcgcggcagccatg gtgcgacgaatgcggctc
<i>AprD4-R</i>	ggtggtggtggtgctcgag tcaggcgtcaccggtcgac
<i>AprD4-E280Q-F</i>	ccggggtgccctggtggtgc CAG acccggtatcgaccggctcg
<i>AprD4-E280Q-R</i>	gcaccaccagggcacccc
<i>AprD4-E303Q-F</i>	gtgcgtcggcgtc CAG gtcggcgtggagagcggcgac
<i>AprD4-E303Q-R</i>	acctggacgccgacgcac
<i>AprD4-R250-R</i>	gaagacggccgcggtgatg
<i>AprD4-R250A-F</i>	catcaccgcggccgtcttc GCT gaccgggtgttctccttc
<i>AprD4-R250M-F</i>	catcaccgcggccgtcttc ATG gaccgggtgttctccttc
<i>AprD4-R250N-F</i>	catcaccgcggccgtcttc AAT gaccgggtgttctccttc
<i>AprD4-R250Q-F</i>	catcaccgcggccgtcttc CAG gaccgggtgttctccttc
<i>AprD4-R250K-F</i>	catcaccgcggccgtcttc AAA gaccgggtgttctccttc
<i>AprD4-Y216-R</i>	cgggcagtagaagcggcacg
<i>AprD4-Y216F-F</i>	cgtgccgttctactgccgTTT ccgctcagcgaggccgcaag
<i>AprD4-Y216H-F</i>	cgtgccgttctactgccgCAT ccgctcagcgaggccgcaag
<i>AprD4-D45N-F</i>	cttctgctgcccccgctc AAT ctgatgcgcctggccggcgt
<i>AprD4-D45N-R</i>	gagcgggggcagcaggaag
<i>AprD4-E220Q-F</i>	ctgccgtaccgcgtcagc CAG ggccgcaagatccgcaccta
<i>AprD4-E220Q-R</i>	gctgagcgggtacgggcagtagaa

Computational studies

The Jaguar program from the Schrödinger suite¹⁷ was used for all quantum calculations. The 2.55 Å-resolution of the AprD4 X-ray model prevented us from using hybrid quantum mechanical (QM) /molecular methods. Instead quantum calculations were performed on a model of the AprD4 active site. We employed the DFT method implemented in the Jaguar program. The B3LYP functional was used with the 6-31G** basis set and the cc-pVTZ(-f) basis set for single point calculations. Calculations were done *in vacuo* as well as with a dielectric of 4 (exceptionally 78 for water); unless specified, all those presented here were performed *in vacuo* as no significant difference was observed. All model representations omit non-polar hydrogens for the sake of clarity except those differentiating the enol from the ketone form (see below). The reaction mechanism of AprD4 starts with the abstraction of a hydrogen atom by the radical 5'dA• that was formed from SAM cleavage (Figure S1). We did not model this first step as we have already characterized it for another radical SAM enzyme.¹² Besides, given the experimental data on AprD4, it is known that, in order to form **2** from **1**, the hydrogen abstraction occurs at C4'.¹⁸ We therefore started from a model with the radical at C4', for which we included the side chains of important residues in direct interaction with paromamine in the crystal structure, namely A27, Y216, R250, E280, E303 and E37. Hydrogen atoms were constructed with the different protonation states we wanted to study. The geometry was then optimized, keeping some of the atom positions fixed (indicated by a * in the various schemes below) to mimic the constraints imposed by the protein matrix.

Ketyl radical formation

Analyzing the crystal structure, Y216 was the only possible candidate to deprotonate the substrate at the O4' position in order to form the ketyl radical (see main text). In the crystal structure, the oxygen atom of the Y216 phenoxyl group is located 3.8 Å away from the D-glucosamine O4' atom (Figure 3b). R250, activated by the insertion of the substrate amine group (N2', see main text) in between E280 and E303, is proposed to deprotonate the Y216 hydroxyl group. Following this hypothesis, we started with a model where Y216 was protonated, R250 protonated, E280 deprotonated, E303 protonated, with moreover a neutral amino group at N2' of **4**, due to the substrate diffusion in a hydrophobic region (Figure S13 and main text for a detailed explanation). Geometry optimizations *in vacuo* as well as with a dielectric of 4 led to a spontaneous deprotonation of R250 and subsequent protonation of E280. Once deprotonated, R250 could in turn deprotonate Y216, which then moves toward atom O4' (Figure 3b). Indeed, an energy scan of the Y216 hydroxyl proton moved from Y216 to R250 shows that the cost is negligible (less than 1 kcal/mol, i.e. most probably spontaneous with thermal fluctuations) and the resulting state is more stable by 2.7 kcal/mol.

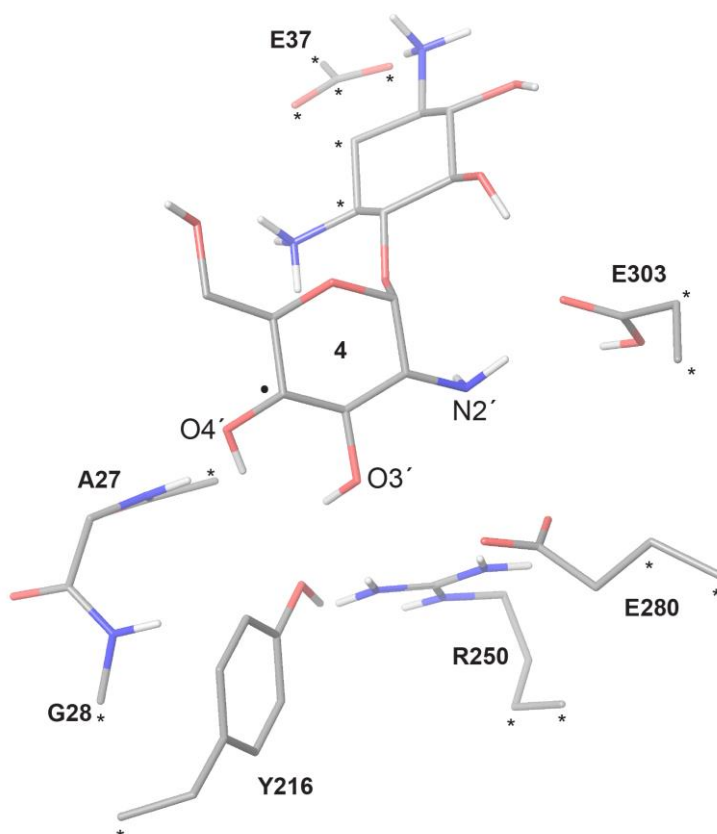


Figure S13. QM starting model of the radical at C4' (**4** in Figure 1b).

Once Y216 is deprotonated, we investigated the possibility of it acting as a base to deprotonate the O4' atom of D-glucosamine thus forming the ketyl radical. We geometry-optimized a tyrosine and a minimal model of paromamine including only the D-glucosamine part *in vacuo* and in water and calculated vibrational frequencies. It

shows that, thermodynamically (see Table below; energies are given in kcal/mol) the deprotonation of O4' by the tyrosine is favored once the radical at C4' is formed, confirming the resulting acidification of this proton.

O4'H deprotonation by Tyr	ΔH_{vac}	ΔG_{vac}	ΔH_{wat}	ΔG_{wat}
Substrate	+5.2	+4.2	+3.8	+4.1
Radical	-12.9	-12.5	-10.5	-9.99

This is in agreement with the fact that the formation of the **4** radical species acidifies O4' to a point where its pKa comes closer to that of a tyrosine residue.¹⁹ Finally, starting from our model where Y216 had shifted toward the O4', we scanned the energy profile of the O4' proton transfer to the O η atom of Y216. The energy cost is 5.2 kcal/mol and the proton transfer onto Y216 results in a stabilization of 5.6 kcal/mol (Figure S14).

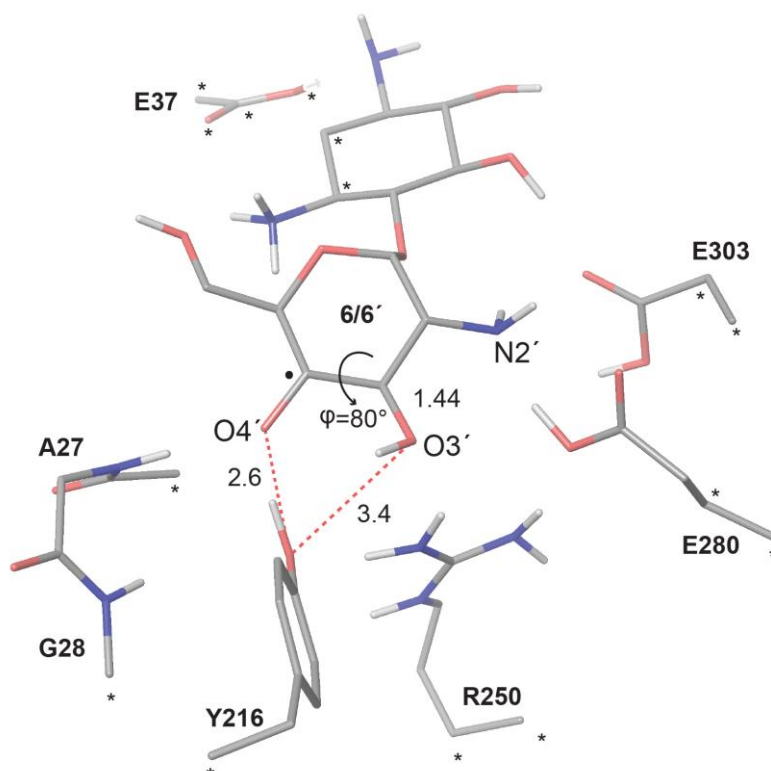


Figure S14. QM geometry-optimized model of **6/6'** in Figure 1b after deprotonation of the O4' atom by Y216.

However, in this conformation, dehydration at C3' catalyzed by AprD4 is not favored due to poor orbital overlap (cf main text and Figure 5). Thus, we investigated the possibility of a conformational change of the D-glucosamine-derived radical that would weaken the C3'-O3' bond.

Radical conformational change

In order to test if other substrate conformations were possible within the active site, we built all the possible puckering geometries described for the D-glucosamine

ring using the 181 conformers of N-acetyl-D-glucosamine that were reported.²⁰ Subsequently, we manually docked them into the active site and filtered them based on the conservation of the position of the C1'-O4 bond (keeping the 2-DOS moiety in place) and of the N2' and O3' atoms. We then excluded all those that exhibited obvious clashes with the protein residues. Among the 181 possible puckering conformations, only two sets passed these criteria. Conformations that were retained are numbered 25, 27, 29, 33, 52, 55, 87, 90, 92, 95, 97, 101, 112, 123, 132, 133, 156 and 169 in reference 20. The first set corresponds to conformations close to the chair conformation of the ring as observed in our crystal structure. The second set corresponds to a boat pucker with the O4' atom moving toward the amino group carried by atom C3 of the 2-DOS fragments (Figure 1a). Interestingly, in the conformations of this latter set, the dihedral angle between the partially occupied p-orbital at the C4' radical center and the σ C3'-O3' orbital (that we called ϕ and the C3'-O3' distance, d3') is about 10° (i.e. well in the periplanar region) maximizing the orbital overlap suitable for fast dehydration (Figure 5). The two sets of substrate conformations were then geometry-optimized using two different models, a first one with an amine at N3 *in vacuo* and a second one with an ammonium at N3 using a dielectric of 4. In both cases the N1 and N2' amino groups were modelled as amine as they are neutralized in the protein by glutamate residue side-chains (E37 and E280, respectively). The N1, O4 and N2' atom positions were constrained during the optimization to avoid spurious conformational changes unreachable in the AprD4 active site. We found three sets of conformations after optimization. The first one (Figure S15, left) was, as expected, very close to the X-ray chair conformation, exhibiting an average ϕ dihedral angle and d3' distance of 78° and 1.42 Å, respectively, close to those of the X-ray-derived radical that we geometry optimized in the AprD4 active site (77° and 1.42 Å, respectively). In the second set, the C5'-O5' bond was broken which we know cannot happen in the AprD4 active site. The third set consists in D-glucosamine distorted boat conformations (Figure S15, right).

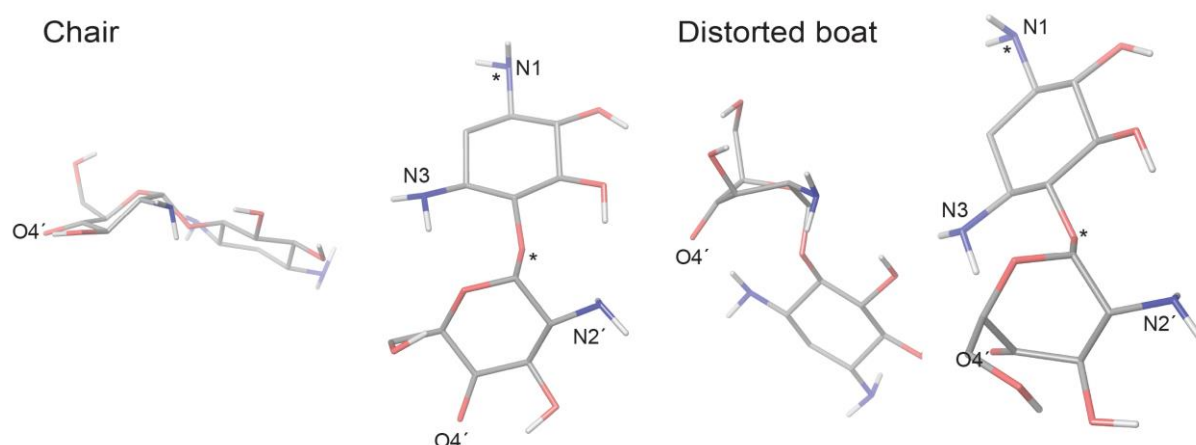


Figure S15. QM geometry-optimized model of the chair (left) and the distorted boat (right) conformations found, from our systematic search for alternative conformations for the C4' radical.

When geometry optimization was performed with the dielectric of 4 and an ammonium at N3, the O4' was protonated by the ammonium during the process resulting into a shortening of d3'; in this case, even if ϕ lies in the periplanar region, the dehydration is still disfavored since the ketyl radical is not formed. We therefore focused on the geometries we obtained *in vacuo* with an amine group at N3; in this case, the average ϕ and the average d3' are 6.2° and 1.47 Å, respectively, values suitable to envisage dehydration. When we geometry-optimized a minimum model of the radical, with only the D-glucosamine part, initially in its distorted boat conformation, it converged toward a chair conformation. Inspecting the intermediate conformations during this conversion from distorted boat to chair shows that it goes, half way (Figure S16), through a half-chair conformation for which ϕ and d3' are 19° and 1.50 Å, respectively, thus satisfying the necessary conditions for dehydration to occur. Conversely, this shows that just initiating a transitory conformational change (through thermal fluctuations) from chair to boat will be enough to dehydrate; thus it no longer becomes a problem if the amino group is protonated, as dehydration will occur well before even reaching the alternative boat conformation.

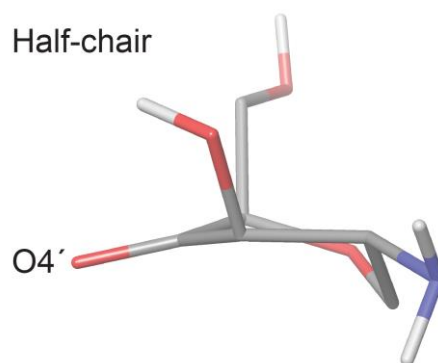


Figure S16. QM model of the intermediate conformation between the chair and the distorted boat conformation.

Dehydration model

The conformational flexibility described above allows the weakening of the C3'-O3' bond; we then constructed small models to evaluate whether E280 could protonate the O3' to release water. We built a model of **6** with the D-glucosamine part in the alternative boat conformation (a limit form to reach the half-chair conformation) and the side-chain of a glutamate residue; we thought E280 could play the role of Cys225 in RNR that is proposed to protonate the hydroxyl group at the corresponding C2' for subsequent water release (see Step S2 in Scheme 1 of reference 21). Initially, ϕ lies in the periplanar region to allow for dehydration; on the first step of the energy scan, the conformation of the D-glucosamine goes from the boat to a half-chair conformation and the radical spin is mainly located on the C4' and O4' atoms with also some radical character at the elongated C3'-O3' bond. The energy scan performed to protonate O3' reveals an energy increase of less than 1 kcal/mol. This shows that, when thermal fluctuations are taken into account, this step will be spontaneous once the conformational change has occurred. We should mention here that trying to form the water molecule with the O4' atom being protonated led to an increase in energy

by 30 kcal/mol with no minimum found, further confirming that ketyl radical formation is essential. After water release, most of the spin is displaced on C3' (Figure S17).

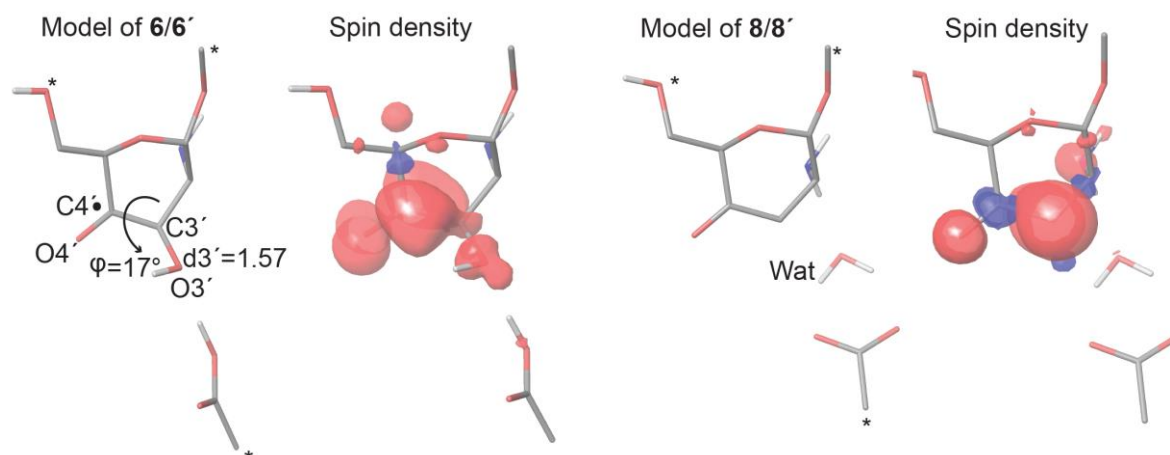


Figure S17. QM geometry-optimized model and spin density of **6/6'** and **8/8'** in Figure 1b after dehydration.

Fate of the radical once the product is formed

Protonation of the dehydrated substrate is necessary to finish the reaction. Once **8** is formed by dehydration, the radical character is no longer on C4' but mostly relocated on C3' (Figure S17). As a consequence, the basicity of the O4' atom is increased and, indeed, we find that a proton transfer from the tyrosine back to O4' is now favored, with concomitant transfer of the radical character onto the tyrosine (and partially on the glutamate) (Figure S18).

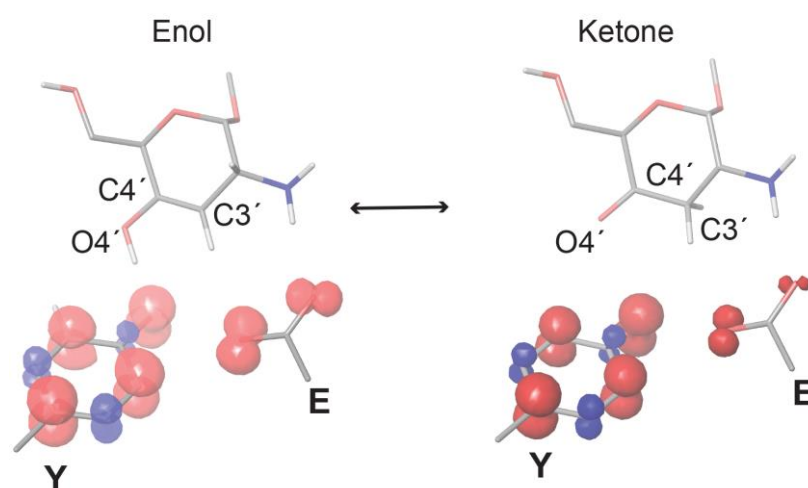


Figure S18. QM model illustrating the fate of the radical once Y216 has protonated the O4'. The spin density shows that Y216 can trap the radical once dehydration has occurred.

References

- (1) Forouhar, F.; Arragain, S.; Atta, M.; Gambarelli, S.; Mouesca, J.-M.; Hussain, M.; Xiao, R.; Kieffer-Jaquinod, S.; Seetharaman, J.; Acton, T. B.; Montelione, G. T.; Mulliez, E.; Hunt, J. F.; Fontecave, M. *Nat. Chem. Biol.* **2013**, 9, 333.
- (2) Goldman, P. J.; Grove, T. L.; Booker, S. J.; Drennan, C. L. *Proc. Natl. Acad. Sci. U. S. A.* **2013**, 110, 15949.
- (3) Lv, M.; Ji, X.; Zhao, J.; Li, Y.; Zhang, C.; Su, L.; Ding, W.; Deng, Z.; Yu, Y.; Zhang, Q. *J. Am. Chem. Soc.* **2016**, 138, 6427.
- (4) Vernede, X.; Fontecilla-Camps, J. C. *J. Appl. Crystallogr.* **1999**, 32, 505.
- (5) Kabsch, W. *Acta Crystallogr. Sect. -Biol. Crystallogr.* **2010**, 66, 125.
- (6) Brunger, A. T. *Nature* **1992**, 355, 472.
- (7) Krissinel, E.; Henrick, K. *J. Mol. Biol.* **2007**, 372, 774.
- (8) Sheldrick, G. M. *Acta Crystallogr. Sect. A* **2008**, 64, 112.
- (9) Pape, T.; Schneider, T. R. *J. Appl. Crystallogr.* **2004**, 37, 843.
- (10) Matthews, B. *J. Mol. Biol.* **1968**, 33, 491.
- (11) Adams, P. D.; Afonine, P. V.; Bunkoczi, G.; Chen, V. B.; Davis, I. W.; Echols, N.; Headd, J. J.; Hung, L.-W.; Kapral, G. J.; Grosse-Kunstleve, R. W.; McCoy, A. J.; Moriarty, N. W.; Oeffner, R.; Read, R. J.; Richardson, D. C.; Richardson, J. S.; Terwilliger, T. C.; Zwart, P. H. *Acta Crystallogr. D Biol. Crystallogr.* **2010**, 66, 213.
- (12) Nicolet, Y.; Amara, P.; Mouesca, J.-M.; Fontecilla-Camps, J. C. *Proc. Natl. Acad. Sci. U. S. A.* **2009**, 106, 14867.
- (13) Nicolet, Y.; Zeppieri, L.; Amara, P.; Fontecilla-Camps, J. C. *Angew. Chem. Int. Ed Engl.* **2014**, 53, 11840.
- (14) Ramachandran, G.; Ramakrishnan, C.; Sasisekharan, V. *J. Mol. Biol.* **1963**, 7, 95.
- (15) Chen, V. B.; Arendall, W. B.; Headd, J. J.; Keedy, D. A.; Immormino, R. M.; Kapral, G. J.; Murray, L. W.; Richardson, J. S.; Richardson, D. C. *Acta Crystallogr. Sect. -Biol. Crystallogr.* **2010**, 66, 12.
- (16) Afonine, P. V.; Moriarty, N. W.; Mustyakimov, M.; Sobolev, O. V.; Terwilliger, T. C.; Turk, D.; Urzhumtsev, A.; Adams, P. D. *Acta Crystallogr. Sect. -Struct. Biol.* **2015**, 71, 646.
- (17) Schrödinger Release 2016-1: Jaguar, Schrödinger, LLC, New York, NY, 2016.
- (18) Kim, H. J.; LeVieux, J.; Yeh, Y.-C.; Liu, H. *Angew. Chem.-Int. Ed.* **2016**, 55, 3724.
- (19) Hayon, E.; Simic, M. *Acc. Chem. Res.* **1974**, 7, 114.
- (20) Mayes, H. B.; Broadbelt, L. J.; Beckham, G. T. *J. Am. Chem. Soc.* **2014**, 136, 1008.
- (21) Nordlund, P.; Reichard, P. *Annu. Rev. Biochem.* **2006**, 75, 681.